remote sensing

MDPI

Article

Using Landsat Image Series to Identify and Characterize Persistent Oceanographic Structures in a Dynamic Marine Protected Area (North of San Jorge Gulf, Argentinian Patagonia)

O. Magalí Olmedo-Masat [1], Juan Pablo Pisoni [1,2], Daniel Rodríguez-Pérez [3,*] and Noela Sánchez-Carnero [1,4]

[1] Centro Para el Estudio de Sistemas Marinos (CESIMAR), CCT CONICET—CENPAT, Puerto Madryn 9120, Argentina
[2] Instituto Patagónico del Mar, Universidad Nacional de la Patagonia San Juan Bosco (IPaM, UNPSJB), Puerto Madryn 9120, Argentina
[3] Departamento de Física Matemática y de Fluidos, Facultad de Ciencias, Universidad Nacional de Educación a Distancia (UNED), 28040 Madrid, Spain
[4] Grupo de Ocenografia Fisica (GOFUVI), Facultade de Ciencias do Mar, Campus de Vigo, Lagoas-Marcosende, Illa de Toralla s/n, 36331 Vigo, Spain
* Correspondence: daniel@dfmf.uned.es

Abstract: Coastal oceanographic processes, like up- and downwelling, topographic fronts, etc., have consequences in biological communities. In some cases, these processes show up as surface structures observable in satellite imagery at different scales. In this work, we focus on the persistent structures observed in the coastal marine protected area of Parque Interjurisdiccional Marino-Costero Patagonia Austral (PIMCPA), one of the most relevant areas of the Argentine coast in terms of biodiversity and productivity. Using 80 Landsat-8 30 m-resolution images from the years 2017–2021, more than 20 structures were identified in the PIMCPA that appear consistently across seasons in approximately the same areas. We focus on four of them, those that are persistent and of medium scale, whose dimensions do not extend in most cases more than 10 km from their region of generation, and describe their location and shape in detail, and analyze their dependence on forcing variables such as tides, wind, bathymetry, and seasonality. Tidal currents prove to be the most significant variable in the formation and evolution of the structures described, above wind or seasonal stratification, which play only a secondary role.

Keywords: marine structures; eddies; tidal currents; Landsat images; Parque Interjurisdiccional Marino-Costero Patagonia Austral (PIMCPA)

Citation: Olmedo-Masat, O.M.; Pisoni, J.P.; Rodríguez-Pérez, D.; Sánchez-Carnero, N. Using Landsat Image Series to Identify and Characterize Persistent Oceanographic Structures in a Dynamic Marine Protected Area (North of San Jorge Gulf, Argentinian Patagonia). *Remote Sens.* **2023**, *15*, 2147. https://doi.org/10.3390/rs15082147

Received: 27 February 2023
Revised: 10 April 2023
Accepted: 17 April 2023
Published: 19 April 2023

1. Introduction

Coastal areas represent around 10% of the total area of the world oceans and, despite their relatively modest surface area, play a considerable role in marine ecology [1]. The coastal area shows a wide range of fascinating and complex fluid motions, leading to rapid biological responses; creating irreversible transports of mass, biomass, and nutrients. Analogous to the structures observable at the ocean basin level (such as the 'gyre' circulation), mesoscale structures can also be observed in coastal areas, being mainly made up of rotating vortices. Furthermore, submesoscale structures (<10 km) are powerful mechanisms for horizontal and vertical mixing, which thus have important biological implications [2,3]. For example, eddies behind headlands and islands do contribute to the increased aggregation and dispersion of larvae and organisms [2].

The study of this zone of interaction of terrestrial, marine, and atmospheric processes depends, to a large extent, on the ability to identify, measure, and analyze the dynamical structures in this zone. Traditionally, different studies have been carried out onboard ships and focused on water quality, nutrients transport, etc. [4,5]. However, the spatial scale of

coastal processes makes it unrealistic to deploy vast resources to record their dynamics in detail [6].

Remote sensing appeared in the late 1850 (mid XIX century) with aerial photography as an alternative or complement of these in situ measurements [7]. The high spatial resolution, as well as the possibility of using multispectral (or even hyperspectral) cameras, made airborne photography a powerful tool for coastal management, including aspects of changes of shoreline features [8,9], censuses for surveying organisms [8–10], etc. Satellite images, although providing a lower spatial resolution than aerial photographs, allow the synchronic acquisition of wide area scenes (in the order of hundreds to thousands of km) and with a moderate temporal resolution (measured as the time of revisit, ranging from minutes, for geostationary satellites, to weeks, for heliosynchronous satellites), whereas aerial photographs just present a snapshot image at a precise time and location, which may not represent the mean condition [11].

Onboard satellite sensors can be optical (using visible and near and medium infrared bands of the spectrum), thermal (using the thermal infrared bands), or radar (using microwaves). The first group is the most used in both terrestrial and marine applications; in fact, the family of ocean color sensors, such as those that measure surface chlorophyll concentration and turbidity, are optical [12–14]. Thermal infrared sensors are used to obtain sea surface temperature in the few upper millimeters [15] often in conjunction with other optical sensors onboard satellites. Additionally, in recent years radar sensors have been applied to estimate surface winds or salinity [16–18], although this requires data integration from wide areas of the ocean, thus drastically reducing their spatial resolution. After decades of research and development, ocean color products from space-borne remote sensing instruments play an important role in managing and monitoring ecosystems, which has allowed more continuous measurements in space and time [19,20].

Despite multiple applications to sea surface characterization, the spatial resolution of the "ocean sensors" (hundreds of meters) is not good enough to study fine structures in coastal areas. On the other hand, multipurpose environmental sensors, such as Sentinel 2 MSI or Landsat 8 OLI, do not possess the best fitting spectral bands to characterize sea water variables. However, these sensor images can still provide useful information about dynamic structures appearing on the surface with the required resolution in coastal areas (tens of meters) [20]. Furthermore, the Landsat imaging series comprehends the longest continuous record of coastal area information (dating back to 1978), also including gradual improved spatial, temporal, spectral, and radiometric resolutions as the satellite series evolved [21]. Early studies often used pairs of images or one single image for only a limited number of years but today, annual or interannual changes can be monitored, due to the availability of free data and improvements in data storage capacity [22].

High-resolution satellite imagery provides a possibility to observe dynamical processes, such as the generation of eddies, mushroom-like current structures, filaments, etc. [23], that reveals the hidden physical dynamics that play an important role in the physical–biological interaction [24]. Since the 1970s, structures such as island wakes and headland eddies in coastal waters were identified from spaceborne and airborne remotely sensed imagery in the visible wavelengths with a spatial resolution of 80 m [25] or through a combination of aerial photography and enhanced terrestrial imagery [4].

Previous studies have shown that some structures observed in remotely sensed images in coastal areas are comparable with ideal flow patterns seen in laboratory experiments. However, observed and predicted length scales do not fit so well for eddies behind the islands (Pattiaratchi et al., 1986 [25]). Furthermore, submesoscale processes (L = 1–10 km, T = 1–10 days) make an important contribution to the vertical mass flux, buoyancy, and tracers in the upper ocean, thus improving the exchange between pycnocline and the surface, playing a crucial role in the processes of stratification on the upper part of the ocean and the mixing layer, developing in a time-scale of days [26].

The characterization of these structures if of high importance in coastal areas, due to the presence of optically active components such as phytoplankton, yellow substance

and suspended sediments [27], which are known to be related to increased aggregation of organisms along the edges of the structures formed [28–30].

Argentina is one of the largest countries in the world, and it has about 5700 km of coastline stretching from the La Plata river estuary to the Beagle channel, and a continental shelf of more than 6.5 million km^2 [31]. Despite the numerous studies on its coastal environments, few studies have analyzed submesoscale processes, mostly of them located in the Patagonian Sea. These regional studies demonstrate that irregular bottom topography, together with unusually large tidal amplitudes and wind stress, condition the vertical structure and generate eddies, gyres, and jets through vorticity [32–36].

San Jorge Gulf (GSJ) is the biggest of Argentinean Patagonian Gulfs, covered by cold-temperate shelf waters resulting from the mixing process between pure sub-Antarctic waters, coastal waters of continental origin and sea-air fluxes. Due to the influence of two tidal fronts it is one of the most productive sectors, and with the highest marine biodiversity in the Argentine Sea [37]. Its Northern part was established in 2007 as marine protected area by the federal and provincial governments, through an agreement between the National Parks Administration and the Government of the Province of Chubut (Law 26446/2008) because it is one of the most relevant areas of the Argentine in terms of biodiversity and productivity [38].

Because of its ecological relevance and high dynamism, this area has been previously studied from different perspectives: seabirds and marine mammals communities [37,39–41], bottom characterization (Sánchez-Carnero et al., 2020 [42]), biological and chemical oceanography [43–48], physical oceanography [45,49–51], even submesoscale processes characterization [32,36]. However, due to its large size, no systematic study of the submesoscale processes of the entire protected area of the northern San Jorge Gulf has been carried out so far.

The aim of this study was to identify persistent submesoscale structures in the northern San Jorge Gulf using Landsat-8 images for a period of five years. After identification, the structures were characterized and classified, and their relationship with the main forcing factors in the area were studied: tide current, wind, and seasonal stratification.

2. Study Area

The study area corresponds to the northern coastal zone of San Jorge Gulf, the largest gulf of the Argentinian Patagonian shelf. This gulf is a semi-open basin with an extension of 39,340 km^2, located between 45°S (Dos Bahías Cape) and 47°S (Tres Puntas Cape) (Figure 1) and with a mean depth of 81 m with a maximum depth of around 100 m, mainly covered by silt with coarse granulometric fractions in the north and south ends of the gulf [52,53]. Circulation within the gulf is seasonally variable, in summer a cyclonic gyre develops in the south of the gulf and a weak anticyclonic gyre in the north; in winter a large anticyclonic gyre is present in the southwestern sect. It is a fishing ground and breeding and spawning area of many fish and crustacean species including commercial shrimp *Pleoticus muelleri* and hake *Merluccius hubbsi* [54]. San Jorge Gulf presents particularly difficult management problems because it is exposed to environmental risks related to oil production: urban-industrial development of the Comodoro Rivadavia hub, prospective offshore drilling, and intense shipping activity [55]. Oil production coexists with major fisheries targeting valuable shrimp, hake, scallops and king crab stocks [56] and with areas of great significance for marine conservation because of the presence of reproductive aggregations and foraging grounds of many marine birds and mammals.

In the northern area of this gulf, the Marine Protected Area *Parque Interjurisdiccional Marino Costero Patagonia Austral* (PIMCPA) was established in 2007 and the trawl fishing was interdicted in 2013 (Figure 1). It is one of the most relevant areas of the Argentine coast in terms of biodiversity and productivity [37,38,57,58] and currently a management plan is being developed in it, involving government and scientific staff. The region encompasses a shallow ecosystem unit of the inner Patagonian Shelf in the Southwestern Atlantic Ocean, an area with depths up to 90 m [59] and including several coastal islands, headlands, and steep slopes, about which detailed information is lacking [36]. It is influenced by the North

Patagonian Frontal System which is forced by seasonal thermal stratification and high energy dissipation of semi-diurnal tides. Semidiurnal tides constitute one of the main ocean forcings of this region, having a typical intertidal range around 4 m [37,60], and due to their seasonality, homogeneous coastal waters remain vertically separated in a stratified water column up to long distances from tshe coast [61,62].

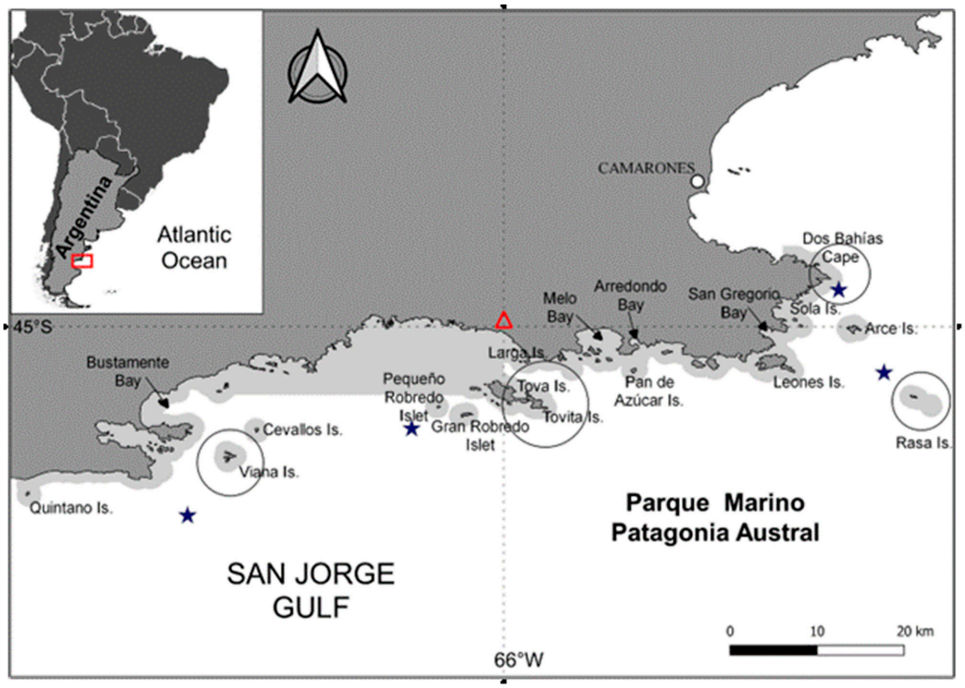

Figure 1. Geographical location of Golfo San Jorge. The *Parque Interjurisdiccional Marino-Costero Patagonia Austral* (PIMCPA) is represented as the hatched area. Red triangle denotes wind node, blue stars show the localization of tidal current nodes, and empty circles signal the mean position of structures described in detail in Section 4.2.

Prevailing winds in the GSJ are from the west, with mean values of 20 km h^{-1} [63]. The closest mean wind speed record, belonging to the National Meteorological Service weather stations, located 27 km north of the PIMCPA, recorded a mean wind speed of 28 km h^{-1} for the period 1971–1980 [64]. The wind action over the gulfs locally affects a thin surface layer through vertical (turbulent) diffusion; for the rest of the domain, wind effects are communicated indirectly through pressure gradients (free surface elevation) and vertical flows generated by the presence of the coast, which blocks horizontal water movement, or by wind-induced upwelling/downwelling events [60].

3. Data and Methodology

3.1. Data Sources

Landsat-8 multispectral images were used to detect and measure the coastal dynamic structures. Landsat images comprehend 9 optical bands (OLI sensor) with a moderate spatial resolution of 30 m [65]. The Landsat-8 scenes corresponding to the PIMCPA study area (227 path-091 row, and 228 path-091 row) were downloaded using the USGS EarthExplorer portal (https://earthexplorer.usgs.gov/; accessed on 26 February 2023), processed at Level 1T, i.e., geometrically and terrain corrected. A total of 80 cloud-free (less than 5%) images spanning the years 2017–2021 were processed for this study.

Tidal current data were obtained from the TPXO tide model which provides both the sea surface height and tidal current vector (eastward (u) and northward (v) components) based on the global barotropic model TPXO9-atlas. The atlas was fitted by the method of least squares to the Laplace tidal equation using both mareograph and satellite data from Topex/Poseidon mission [66]. The TPXO model provides both the sea level and tidal

current vector (u,v components) based on the global barotropic model TPXO9-atlas. Time data series corresponding to four nodes in the study area and spanning the same 2017–2021 period were downloaded from the TPXO portal (https://tpxows.azurewebsites.net/; accessed on 26 February 2023) (see Figure 1).

Wind velocities were obtained from the European Centre for Middle-range Weather Forecast (ECMWF) ERA5 reprocessed hourly data [67]. ERA5 provides, among other atmospheric variables, wind velocity components (speed and direction) 10 m above the surface in a ~31 km global grid over the period from 1950 onwards. Time data series corresponding to one node in the study area (Figure 1) for the 2017–2021 period were downloaded from the Copernicus Climate Data Store (https://cds.climate.copernicus.eu/; accessed on 26 February 2023).

Detailed bathymetry data were obtained from a previous work [53].

3.2. Methodology

The methodology consisted of three steps: (1) image masking (clouds) and correction (atmospheric and sunglint) and multi-band visualization adjustment, (2) structure identification and classification, and (3) analysis of structures related with geographical (geomorphology) and forcings variables (tidal currents, winds).

3.2.1. Image Correction and Visualization Adjustment

Since downloaded images were L1P (geometrically and terrain corrected), preprocessing consisted of the reflectance calculation (automatic TOA reflectance calibration and dark object subtraction [68], sunglint correction (NIR-VIS [69], and land and cloud area masking. To carry out sunglint correction, infrared reflectance was used to correct the blue, green and green bands by subtracting pixel-by-pixel the fraction of their reflectances that were linearly correlated with the NIR reflectance in a deep water region [70]; since infrared wavelengths are almost completely absorbed by water, the computed deep water reflectances were assumed to be mostly the effect of sunglint in all optical bands.

Regarding land masking, ad hoc NIR thresholds were established for each image based on histogram modes; land masks were defined as pixels with NIR levels above those thresholds. Cloud masking was applied using two flags and provided in scene metadata: cloud high and mid, and cirrus high and mid.

All these processes helped to maximize the observable radiometric differences on the sea surface of the study area and were performed using SNAP—ESA Sentinel Application Platform v8.0 (http://step.esa.int; accessed on 26 February 2023). After band correction, the blue (450–510 nm), green (530–590 nm), and red (640–670 nm) bands were histogram-equalized over the sea surface to optimize the visualization of marine structures [71].

3.2.2. Structure Identification and Classification

All structures observable in the images of the study area were visually classified according to their shape, following Ivanov and Ginzburg [3]: spiral eddies of the open ocean, eddies behind the islands, eddies near capes, chains of shear eddies, eddies in areas of flow confluence, spin-off eddies, core rings, associated eddies and mushroom-like currents. Then their sizes (length, gyre radius, spatial wavelengths, etc.), sense of rotation (cyclonic or anticyclonic), spatial (region of the study area, distance to the coast, etc.) and seasonal distributions were characterized in order to establish patterns and assess potential triggers.

After the previous characterization, four areas inside the PIMCPA limits were selected for an in depth study, because of their persistence over time: (A) a dipole vortex in the NE sector (near Dos Bahías Cape), (B) a chain of eddies in the E sector (originated around Rasa Island), (C) island wakes in the central sector (originated around Tova and Tovita islands), and (D) eddies in the SW sector (originated near Viana island) (Figure 1).

3.2.3. Data Analysis: Related Variables

Several forcing variables were related with the presence and characteristics of the structures studied in the four areas: tidal current direction and cycle, moon phase index (as a proxy for spring/neap tide amplitude modulation), wind and seasonality (as a predictor of thermal stratification).

The tidal current is complemented with an index (i) and considered to quantify the tidal current velocity modulation in the spring-neap cycle: the index takes the value 1 at spring tide (tidal current is maximum at spring tides), value 0 at neap (tidal current is minimum at neap tides), and intermediate values corresponding to the days near spring tide (values less and close to 1) or near neap tide (values greater and close to 0).

Similar plots (direction and amplitude, 12 + 1 h) were calculated for winds using ERA5-reprocessed hourly data. However, given that wind forcing was not found relevant for structure development, and for the sake of clarity, these plots were not included in the results. All these computations and their representations were performed with the statistical software R (Team, R. C. 2022).

As explained above, a visual analysis of each of the 80 available images was performed, identifying the ocean structures present in them. In the four areas of interest defined within the study area (Figure 1), together with the identification and characterization of the structures (direction and dimensions), the value of the forcing variables was reviewed. This detailed review made it possible to identify which of these variables correlated with the formation of the structures (i.e., directly and consistently throughout the study period); for which purpose, tables were constructed representing the different possible synoptic situations (see tables in Section 4.2). Beyond this, no other statistical adjustment was made for two reasons: first, to avoid the dimensionality error derived from characterizing complex structures through simple numerical variables (for example, using an eddy to define its direction of advance, with a static image, and its dimension, with diffuse ends) and second, because a single variable was shown to be the main forcing agent in practically 100% of the cases, so it was not considered necessary.

4. Results and Discussion

4.1. Observed Coastal Oceanographic Structures in PIMCPA

Similar to what [3] described in their tables in Section 4.2.1, six structures with particular characteristics were considered in this work. These were eddies, vortex streets, spiral eddies of the open ocean, associated eddies chains, eddies behind island (or standing eddies), and dipole vortex or mushroom-like associated with jets. These structures are illustrated in Figure 2, and the reader is referred to it to follow this section. Other structures observed were not classified into any of these typologies due to their complexity.

Regarding the structures' distribution, the entire PIMCPA shows observable structures throughout the study period, with no significant differences in the different seasons, revealing the high dynamism of the area on the sea surface throughout the year.

The structures that were observed in more different locations inside the PIMCPA were the **isolated eddies**. These structures are present throughout the PIMCPA and have been observed recurrently in at least ten locations (associated with the Islands Arce, Leones, Blanca, Tova, Tovita and Gran Robredo Islet; bays such as Gregorio, Melo, Arredondo, Bustamante and Dos Bahías Cape) (Figure 1). Eddies are characterized by their marked spiral form associated with the shear of the horizontal velocity which may correspond to a cyclonic gyre (clockwise in the southern hemisphere) or anticyclonic (counterclockwise in the southern hemisphere) [3] (Figure 2A,B). Their formation in our study area appears to be associated with some geographical features of the coast or some islands that cause the deviation of the surface current generating relative vorticity, similar to that observed by [3]. These structures have been observed with sizes between 0.5 and 7.6 km, measured between the center and the outer end of the eddy. They appear in 100% of the images studied, and their persistence is very high throughout the study area with perhaps the exception of the Dos Bahías Cape, Arce Is. and Leones Is. areas, where some other structures are observed

instead, even more frequently than eddies. In Dos Bahías Cape, where eddies are located, we can observe mushroom-like structures in 58% of the images. In Arce Is., isolated eddies are observed only in 19% of the images, showing eddies behind the island in most cases. Finally, in Leones Is. isolated eddies, eddies behind island and mushroom-like structures appear with similar frequencies.

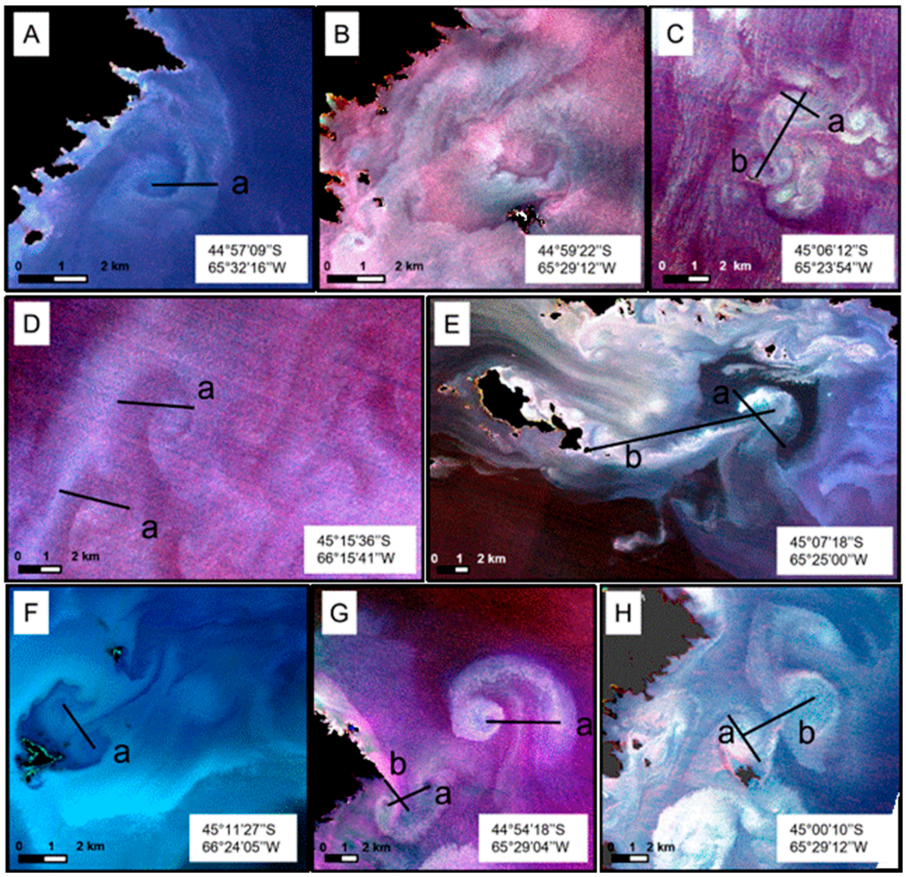

Figure 2. (**A**) Isolated cyclonic Eddy, (**B**) isolated anticyclonic Eddy, (**C**) von Karman vortex street (**D**) spiral eddies of the open ocean, (**E**) mushroom-like currents with shed, (**F**) eddies behind the islands, (**G**) double mushroom-like currents, (**H**) associated eddies. The black lines indicate how the structures were measured and show (a) eddy width, (b) wavelength of the eddies in (**C**,**H**); (a) cap and (b) stem of mushroom-like patterns in (**E**,**G**).

When these eddies appear in groups of two facing each other with opposite turns, both inward, associated with islands, they are called **eddies behind islands** [3], standing eddies, or island wakes [4,25] They occur due to the horizontal shear of the current velocity in the lee of the island when a stream flows around it, slowing it down [3] and can play an important role in heat, freshwater, and mass transports [72].

The structure size/dimensions of the current varies qualitatively, depending on the flow velocity and island cross section (Figure 2F) [3]. In agreement with [25] and [4], the size of the structures is related to the size of the island. Eddies formed in relation to islands that are 1.5 km wide and long, such as Arce and Viana, measure between 1.4 and 5.8 km after its full tidal current phase (6 h). In islands smaller than 1 km in length and width, such as Is. Sola, Pan de Azúcar, or Cevallos, the eddies detected ranged between 0.5 and 2.2 km. This structure is more persistent in the larger islands (almost observed in 100% of the images), however, in Pan de Azúcar Is. it was also persistent (82%) in relation to the smaller ones (44.3% Is. Cevallos and 30.6% in Is. Sola).

Other structures involving two eddies, called "**mushroom-like patterns**", are observed as a dipole associated with a jet, which originates in the flow acceleration of the

incoming current caused by funneling, either passing through a strait between two islands or an underwater channel or past a shallower area [3,73]. This structure is observed around Leones Is. (in 75% of the images), due to an abrupt slope in the bathymetry, Tovita Is. (22%) (Figure 2E) or at Dos Bahias Cape (58%). The distance between the centers of the dipoles varies between 1.6 km and 6.5 km and the dimension of the jet range is between 2 and 11 km (Figure 2G). Although in most cases the length of the jet is smaller than the cape, in agreement with the studies of [73], both are in the same order of magnitude, while the width of the jet does not exceed 10–25% of its length. Only in the case of Tovita Is. mushroom-like structure, the jet length is 2 or 3 times bigger than its cape, especially in spring and summer (see next section).

In the case of Dos Bahías Cape, in some images (around 33% of the images) together with the main mushroom-like structure another mushroom-like structure is observed, parallel to the main one, and in a northerly direction (Figure 2G), probably generated because of the previous tidal current (Pisoni et al., submitted).

Other structures observed were the **associated eddies chains**, characterized by the fact that their eddies turn always in the same direction, i.e., all clockwise or all counter-clockwise [3] (Figure 2H). The chains of shear eddies were observed in two regions of the PIMCPA, always related to Rasa and Tovita islands; the number of eddies in a chain varies from 2 to 6, and the length of the chain varies between 5.6 and 15.5 km.

We also found a group of associated eddies but, in this case, alternating their direction of rotation. This structure is known as **von Kármán vortex streets**, a distinctive pattern that can occur when a fluid passes a tall, isolated, stationary object. In the ocean, this pattern can be seen when the tidal current collides with an island [25]. Two sectors have been detected where street vortices form, the first one related to San Gregorio Bay, as a result of the collision of the tidal current with the small islands in the bay, and the second one associated with Rasa Is., a small island located farther from the coast to the east of the PIMCPA (Figures 1 and 2C). Chains of various sizes were observed, formed by 3 or 5 vortices with a length ranging from 5 km to 10 km, approximately, in general, being the largest ones related to the latter island.

The last classified structure, the **spiral eddies of the open ocean**, were observed in 18% of images in the PIMCPA located around 45.25°S and 66.25°W, mostly cyclonic. These solitary spiral eddies are broadly distributed over the world's oceans, mostly cyclonic, with diameters less than 30 km, and, as [3]) mentioned, detected in areas where there is no shear flow or it is weak. There are not many antecedents on the detection of these spirals in the Argentinean Sea but they have been previously observed in the region of the Brazil-Malvinas confluence by means of SAR images [74]. In our region, the sizes of these gyres (from inner to outer border) ranged between 3.5 and 9.5 km (Figure 2D). The size of ocean eddies varies according to the Rossby radius with the latitude; in low latitude regions, near the equator, eddies are much larger than in high latitude regions [75,76].

4.2. Oceanographic Structure Description: Forcing and Behavior

Four areas were selected in the PIMCPA where structures with relevant spatial scale and persistence over time were observed (Figure 2C,E–G).

Of the four variables whose potential effect on the appearance and size of the structures was studied, only the tidal current showed a significant relationship, observable in the four areas studied. In all cases, not only the direction of the tidal current marked the direction of the structure, but the structure definition in the image (how well developed it showed) was related to the time since the last tidal current direction change prior to image acquisition.

Although the phase of the moon has an important effect on the magnitude of tidal current amplitude, no variation in either the size or development of the structures was generally observed. An effect of the wind was not apparent, even when the wind speed reached high values (>50 km/h) and in the opposite direction to the tidal current.

The few exceptions to these general patterns are detailed in the description of each structure.

4.2.1. Mushroom-Like Structure in Cape Dos Bahias

The first structure studied is generally observed in the form of a dipole (mushroom-like pattern) located at the northeast end of the PIMCPA, between 1.6 and 5.3 km wide (measured as the distance between the gyre centers) (Figure 3A,B). Sometimes, instead of the mushroom-like pattern, an isolated eddy is observed, 0.8 to 6.4 km in size (measured as the largest radius of the structure) (Figure 3C,D). This structure is formed by the interaction of tidal currents with Dos Bahías Cape, a cape 7.5 km north-south and 2 km east-west (Figure 3A). In all the images analyzed, it was possible to identify a mushroom-like pattern or an isolated eddy (Table 1).

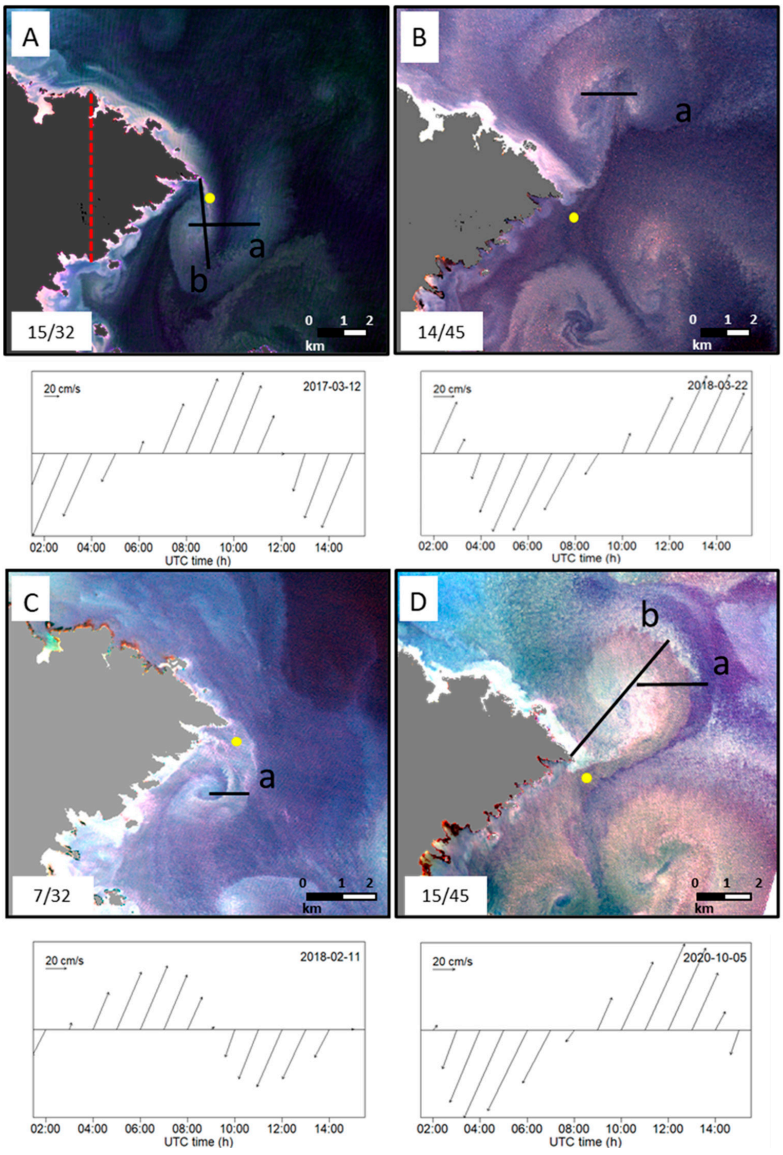

Figure 3. Structures in Dos Bahías Cape (DBC), the red line shows the measured point for the North –South dimension. (**A**) Mushroom-like pattern south of DBC, after 2 h of SSW tidal current. (**B**) Mushroom-like pattern north of DBC, after 5 h of NE tidal current. (**C**) Cyclonic isolated eddy south of DBC, after 5 h of SSW tidal current. (**D**) Anticyclonic isolated eddy north DBC, after 6 h of NNE tidal current. Black lines indicate how the structures were measured, being (a) width of mushroom-like patterns or isolated eddies and (b) distance from Dos Bahías Cape. Numbers in the lower left corner represent the number of scenes showing this particular structure (linked with Table 1). The arrow time series below each image represents the tidal current velocities 12 h prior to the acquisition of the image as extracted from TPXO data at the locations marked by yellow points on the corresponding image.

Table 1. Isolated eddies and vortex dipole in Dos Bahías Cape. Time shows the time during which the tidal current had a consistent direction before image acquisition (in hours). Arrows indicate the predominant direction of the tidal current, disaggregated for each type of structure and direction. Distance between structures and Dos Bahías Cape is also indicated. Finally, several images where each structure is observed are included.

Time (h)	↑	↓	Distance to Cape (km)		Images	
			min	max	↑ (45)	↓ (32)
<4			1.6	3.5	14	15
			1.5	1.8	6	4
≥4			2.8	5.3	10	6
			0.8	6.4	15	7

According to the time elapsed, t, since the last tidal current rotation, this structure passes periodically through different phases: appearance, evolution, restructuring, and disappearance. The distance between the centers of the dipoles visible at each stage varies between 2.7 km and 5.9 km and the dimension of the jet ranges between 3.9 and 7.6 km (Figure 2G), separating from Dos Bahías Cape up to 13 km.

The structure has shown a high dependence on tidal current, being located north of Dos Bahías Cape (with a counterclockwise turn to the west and a clockwise turn to the east) when tidal current flows in a northerly direction (Figure 3B,D, Table 1), and south of the Cape (with a clockwise turn to the west and a counterclockwise turn to the east) when the tidal current flows south (Figure 3A,C, Table 1).

In addition to direction, two other aspects of the tidal current were analyzed: the time window prior to image acquisition during which the tidal current presented the same direction (t; Time in Table 1) and the intensity of the current associated with the spring-neap cycle (i). As expected, along with t, the distance from the end of the structure to the tip of Dos Bahias Cape grows, as well as the distance between the eddies. The boundaries of the mushroom-like pattern begin to become fuzzy when t is greater than 4 h. This behavior is independent of the direction of the tidal current, that is, it occurs for both the southward and northward flow. With respect to the current intensity index (i), no effect on the structures is observed.

In 32 images (~41.55% of the total analyzed for this region) an isolated eddy was observed, together with the jet as in the mushroom-like pattern structures, but in the absence of a second gyre. This eddy exhibits the same behavior as the mushroom-like pattern in relation to the tidal current and t. No pattern has been found to relate the variables studied with the appearance of one type of structure or the other (isolated eddies or mushroom-like patterns).

Finally, in 26 images (~34%), a mushroom-like pattern parallel to the main one could be observed south of Dos Bahias Cape, generally larger and in a northerly direction, probably formed by the influence of tidal currents opposite to the one happening at the time of image acquisition (Figure 2G) [36].

4.2.2. Associated Eddies Chain in Isla Rasa

The second structure studied was an associated eddies chain developed behind Rasa Island, at the east of the PIMCPA. It consists of a row of eddies (between 2 and ~10 gyres) that move mainly according to the direction of the tidal current, due to the interaction of marine currents with the island and was observed in all the images analyzed. Although Rasa Is. has dimensions of 0.88 km long and 0.24 km wide, it gives rise to one of the most

turbulent regions in the area. This associated eddies chain extends along 2 to 19 km and shows a width (maximum distance across the chain) that varies between 4 and 11.5 km, in a zone with depths of up to 85 m.

Eddies always move in the same direction of the tidal current: to the north or northeast of Rasa Island if the tidal current flows in a northerly or northeasterly direction (Table 2, Figure 4A,C), and to the south or southwest if the tidal current flows south or southwestwards (Figure 4B,D). On some occasions, this structure develops in the form of von Kármán vortex streets, while on others the width appears to be much greater, and the pattern is not so evident.

Table 2. Eddy group in Rasa Island (black shaded areas). Time shows the time during which tidal current had a consistent direction before image acquisition (in hours). Arrows indicate the predominant direction of the tidal current, disaggregated for each type of structure and direction. Distance between the center of Rasa Island and the farthest end of the associated eddies chain is also indicated. Finally, the number of images where each structure is observed are included.

Time (h)			Distance to Island (km)		Images	
			min	max	(19)	(13)
	↗	↙			↗	↙
1–2	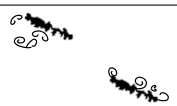	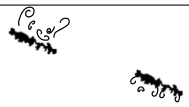	7.0	15.5	6	3
3–4			6.1	11.4	9	5
5–6			5.6	13.1	4	5

As with the previous structure, the tidal current, characterized by t and i, was analyzed. Again, the structure size (length and width of the eddies chain) grows with increasing t, as well as the distance between the eddies forming the chain (they are moving apart with time as the structure develops). The eddies are observed in the process of formation (smaller dimensions and closer to the island) in images with tidal current persistence <2 h and their limits become blurred when t becomes greater than 4 h (Figure 4A–D). In some images, eddies are observed disassembling in the opposite direction, probably as a result of the previous tidal currents (Figure 4B,D). With respect to the current intensity index (i), no clear effect on the structures has been observed.

4.2.3. Eddies behind the Islands in Isla Viana

The third chosen location is a small island 1.5 km long and 1 km wide located in the southwestern region of the PIMCPA, Viana Is. (Figure 1). Due to the interaction of the tidal current with the island, a wake is generated and formed behind it (leeward). Nearby, to the northeast, is another small island, 0.6 km long and 0.2 km wide, Cevallos Is., where eddies are also observable, but of a smaller size.

This wake is observed as two vortices in the lee of the island rotating in opposite directions, and generally similar in size. The distance between the centers of the eddies is about 1 km, although it reaches up to 4.5 km (with southwards tide current flowing past 6 h). The structure has a very high persistence, being present in 100% of the images.

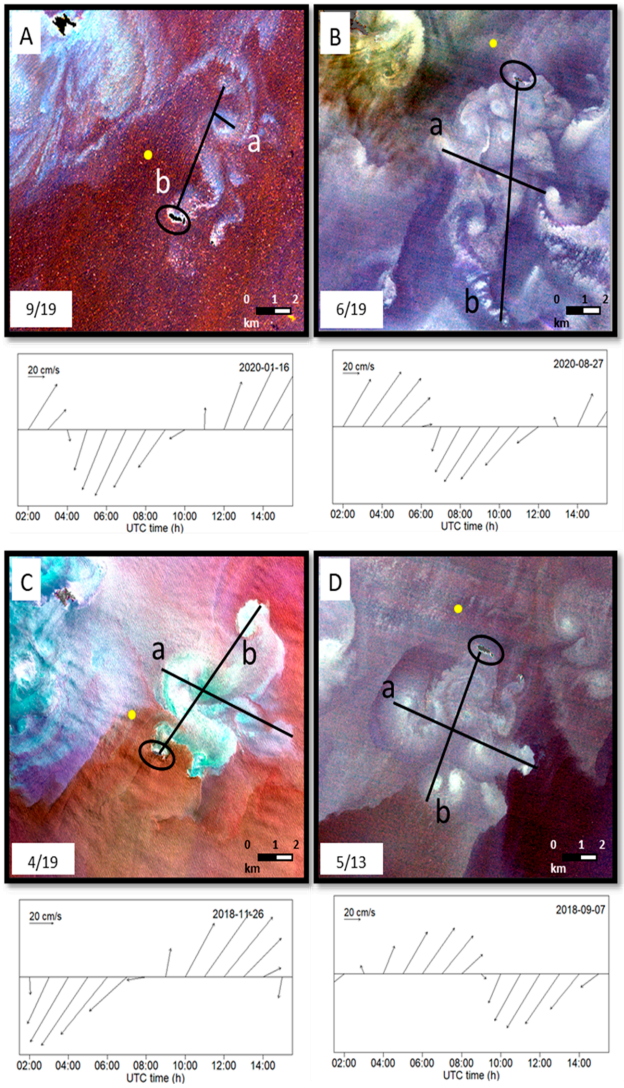

Figure 4. Structures in Rasa Island (inside the black circle). (**A**) Associated eddies chain north of Rasa Is., rotating clockwise, after 4 h of NNE tidal current. (**B**) Associated eddies chain south of Rasa Is., rotating clockwise, after 1 h of N tidal current. (**C**) Associated eddies chain north of Rasa Is., with both rotating directions, after 6 h of NE tidal current. (**D**) Associated eddies chain of Rasa Is., rotating clockwise, after 5 h of SW tidal current. Black lines indicate how the structures were measured, being (a) width of associated eddies chain and (b) distance from Rasa Island. Numbers in the lower left corner represent the number of scenes showing this particular structure (linked with Table 2). The arrow time series below each image represents the tidal current velocities 12 h prior to the acquisition of the image as extracted from TPXO data at the locations marked by yellow points in the corresponding image.

The eddies behind the island show a high dependence on the tidal current direction, always forming downstream (in the lee) of Viana Is. (Table 3, Figure 5). When the tidal current began to turn shortly before image acquisition ($t < 2$ h), it can be observed how the wake starts to form in the same direction of the tidal current (Figure 5B, and sometimes eddies are observed breaking apart in the opposite direction, product of the previous tide (Figure 5A,C). The distance between the eddies increases as the time increases since their generation (Table 3). No effect of i nor seasonality was observed on the structures.

Table 3. Eddies behind Viana island (black shaded areas). Time shows the time during which the tidal current had a consistent direction before image acquisition (in hours). Arrows indicate the predominant direction of the tidal current, disaggregated for each type of structure and direction. Maximum and minimum distance between the center of eddies is also indicated. Finally, the number of images where each structure is observed is included.

Time (h)			Distance between Eddies (km)		Images	
			min	max	(31)	(30)
	↗	↙			↗	↙
1–2			1.1	3.3	7	17
2–4			1.4	3.8	13	8
4–6			1.8	4.5	11	5

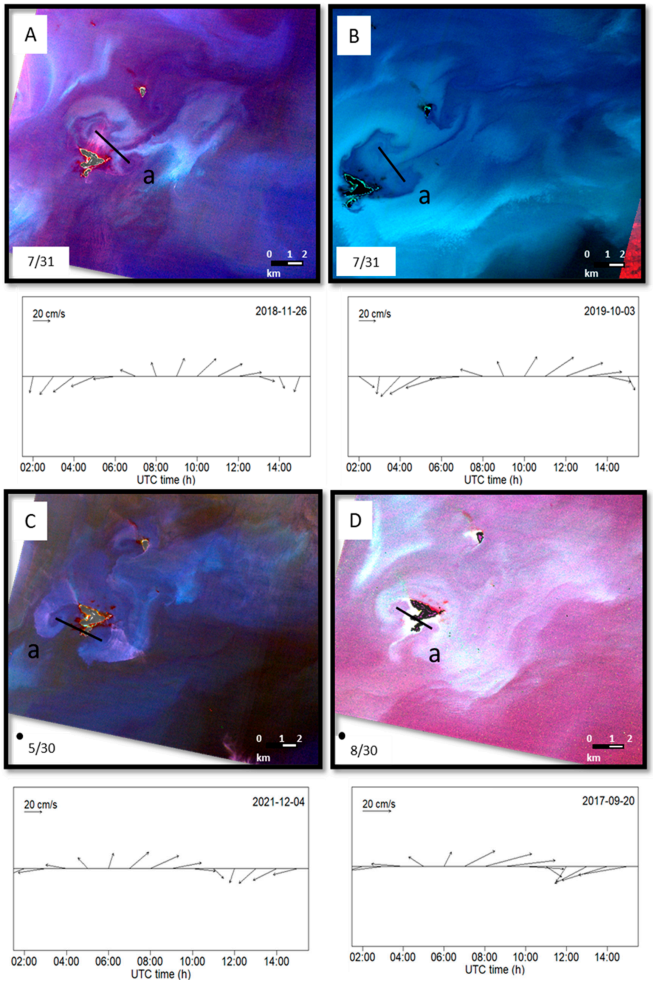

Figure 5. Eddies behind Viana island. (**A**) Eddy north of Viana Is., after 2 h of SE tide current. (**B**) Eddy north of Viana Is., after 1 h of ESE tidal current. (**C**) Eddy south of Viana Is., after 5 h of SW tidal current. (**D**) Eddy south of Viana Is., after 4 h of WSW tidal current. Black lines indicate how the structures were measured, being (a) distance between the eddies' centers. Numbers in the lower left corner represent the number of scenes showing this particular structure (linked with Table 3). The arrow time series below each image represents the tidal current velocities 12 h prior to the acquisition of the image as extracted from TPXO data at the locations marked on the corresponding image.

4.2.4. Island Wake, Associated Eddies Chain, and Mushrooms in Tova Island

The last location selected is in the center of PIMCPA, around Tova and Tovita islands. Tova Island is the largest island in the PIMCPA (~5 km long and 2 km wide) and Tovita Island is 2.3 km long and 1.5 km wide.

In this area, three different structures are observed. An island wake generates eddies behind the island, with cyclonic and/or anticyclonic eddies of different sizes, which generally form leeward of Tova and Tovita islands. This structure is observable in all the images analyzed and shows a high dependence on the tidal current, always growing in the direction of the tidal current (Table 4, Figure 6B,C).

Table 4. Island wake in Tova Is. (black shaded areas). Time shows the time during which the tidal current had a consistent direction before image acquisition (in hours). Arrows indicate the predominant direction of the tidal current, disaggregated for each type of structure and direction. Distance between the center of Tova Is. and the farthest end of the structure is also indicated. Finally, the number of images where each structure is observed are included.

Time (h)			Distance to Island (km)		Images	
			min	max	(31)	(43)
	↗	↙			↗	↙
1–2 h			2.5	13.4	14	18
3–4 h	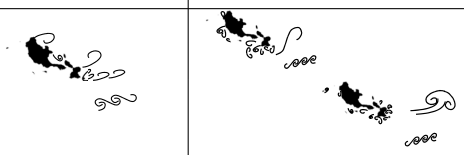		1.3	10.4	2	19
5–6 h		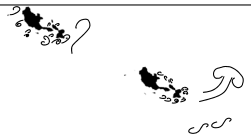	5.2	9.7	15	6

Together with this wake, in 30% of the images, an associated eddies chain is also observed to the east of Tovita island. When the tidal current has started to turn shortly before the acquisition of the image ($t < 2$ h), it can be observed how the structure starts to develop. Generally, it is observed that when t is maximum (6 h), the distance of the larger eddies to Tovita island is greater, always to the east, east-southeast, or southeast directions. This behavior is independent of the direction of the tidal current.

Finally, a peculiar structure observed in this area is a dipole to the east of Tovita Island (23.3% of the images), growing always in east or east-southeast direction, reaching up to 13.5 km off the island shores, and with a jet that even reaches 11 km. The appearance of this structure is independent of the tidal current direction (Figure 6C,D). The origin of this structure could be a 10–15 m deep wall present in this location (east of Tovita Is.), which induces an inhomogeneity in the bottom stress thus generating the wake vorticity [77], notwithstanding the eastwards mean flow in the zone, mainly during the warm seasons [51].

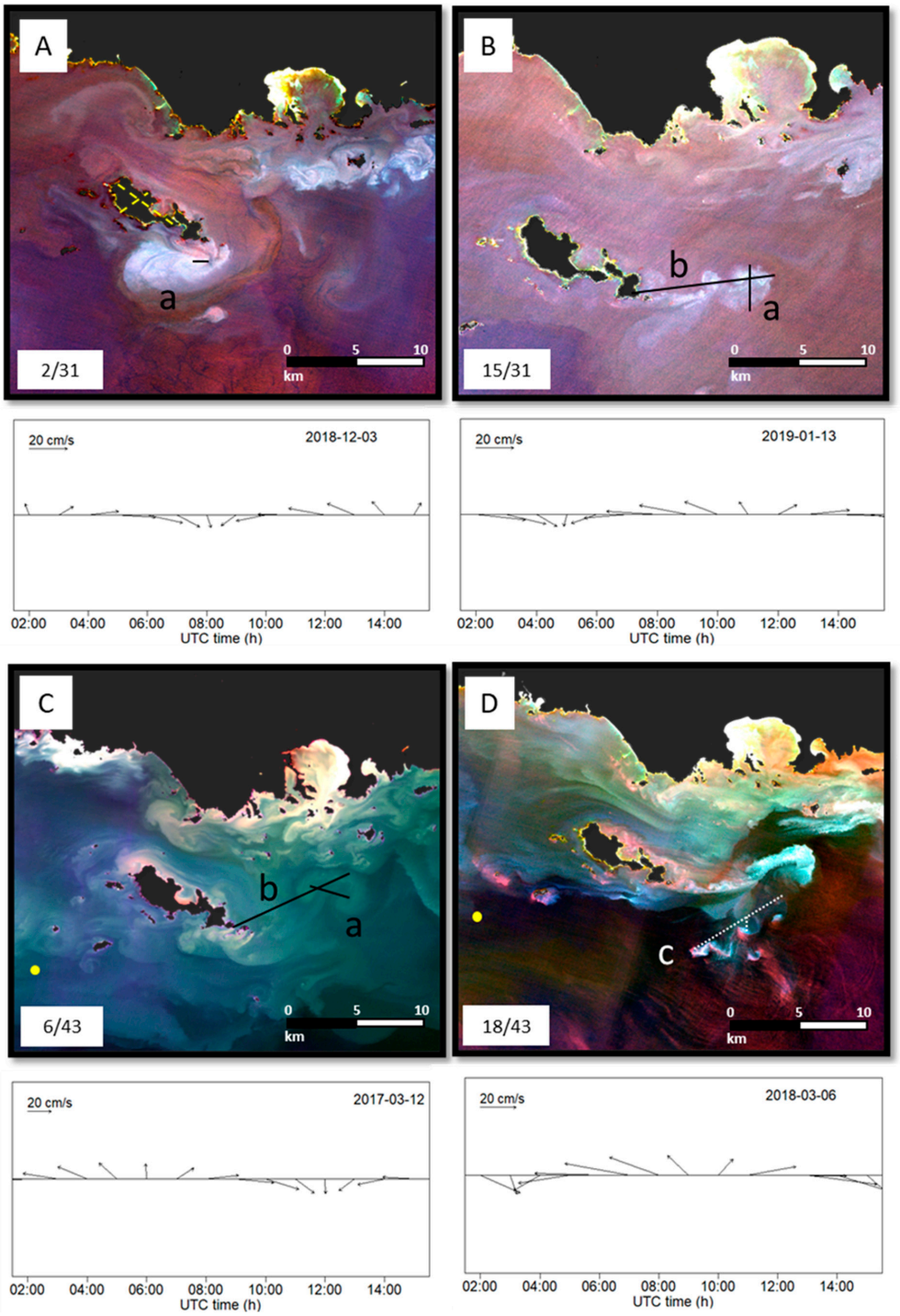

Figure 6. Structures associated with Tova and Tovita islands. (**A**) Cyclonic eddy south of Tovita Is., after 4 h of WNW tidal current. (**B**) Associated eddies chain northeast of Tovita Is., after 6 h of N. tidal current. (**C**) Eddies south and dipole with a jet to the northeast of Tovita Is., after 5 h of S. tidal current. (**D**) Eddy south of Tova and Tovita Is., dipole with a jet to the northeast and chain of eddies to the southeast, after 1 h of ESE tidal current. Black/white lines indicate how the structures were measured, being (a) width of eddies, dipole, or eddies chain, (b) distance from Tovita Is. and (c) length of associated eddies chain. Numbers in the lower left corner represent the number of scenes showing this particular structure (linked with Table 4). The arrow time series below each image represents the tidal current velocities 12 h prior to the acquisition of the image as extracted from TPXO data at the locations marked by yellow points on the corresponding image.

4.3. Methodological Approaches

The present work has taken advantage of images from a medium spatial resolution multipurpose satellite (Landsat 8) to identify and monitor the sub-mesoscale structures in a coastal area over a period of five years. Oceanographic satellites provide data on ocean color, sea surface temperature, sea surface salinity, etc. [12,78–80]. Ocean color sensors, due to their many bands and the fact that they have been specifically designed for studies in the sea, allow the detection of mesoscale and even larger scale oceanographic processes (of the order of 100 km) [24,81] or even at submesoscale levels by applying models derived from vector geometry [82]. However, due to their low spatial resolution (several hundred meters), they are not appropriate for studies of coastal waters where submesoscale structures are of horizontal scales in the order of 1–10 km and time scales in the order of 1 day [26,83]. Although there are new satellites with ocean color capabilities at higher spatial resolutions that can be used in these areas [84], these alternatives are still very few. In this work, the images from the multipurpose Landsat and Sentinel-2 satellite images, with a medium spatial resolution (30 and 10 m respectively), have been a good alternative, allowing, despite having less and wider bands, detailed studies of coastal processes at the sub-mesoscale level [4,23,25,85].

Previous studies have described coastal processes with much higher spatial resolution (in some cases as high as 3 m) using Synthetic Aperture Radars (SARs) [3,86–89]. This high spatial resolution is added to the fact that SAR images are neither affected by the presence of clouds nor the time of day (sun zenith angle). High frequency coastal radars also allow the study of these processes with even greater spatial detail, although these in situ measurements are limited in regularity as their operation requires costly financial and human resources [90]. Moreover, because they only cover the microwave region, SAR imaging methods only provide information on variations in water surface roughness related to wind or the presence of surfactants [3,75].

However, although in some cases some information about the presence of oceanographic fronts can be inferred from roughness differences, in general SAR images do not provide information about substances vertically transported by those fronts, such as chlorophyll, dissolved organic matter, etc., which in coastal sub-mesoscale processes affect biological productivity near the surface, and are easily detectable in the visible spectrum [24,36,83].

5. Conclusions

The present work represents an advance in the understanding of the dynamics of one of the most complex regions of the Patagonian coast, evidenced by the presence of multiple submesoscale structures observed in remote sensing images, which probably give rise to one of the regions with the greatest biodiversity on the Argentine coast.

More than 20 persistent structures were observed in a time series of five years for the marine area of the PIMCPA (an area of around 700 km^2). These structures were classified mainly into six groups (eddies, vortex streets, spiral eddies of the open ocean, associated eddies chains, eddies behind island or standing eddies, and dipole vortex or mushroom-like associated with jets), although other structures with less persistency in the area were also observed. Structures appeared throughout the study period and along the entire PIMCPA and were especially linked to the islands and headlands present in the area. Quantitatively, the highest activity was observed in the easternmost area of the PIMCPA, near Dos Bahías Cape, probably because of the size of the cape and the dynamic tidal current. In this region, the tidal currents appear to be quite reversible (they flow six hours to one side and then reverse direction), while to the west and center of the PIMCPA, the currents are more associated with ellipses with clockwise rotation (see Figures 3–6 and [49]). All structures fell in the category of submesoscale structures, with sizes that rarely exceeded 10 km. The largest structures detected reached 15.5 km in the region of Rasa Is. (associated eddies chain) and 14.3 km in the region of Tovita Is. (mushroom with jet).

All observed structures in the study area were found to be strongly linked to the tidal current, ruled by its direction, duration (measured from tide turn until scene acquisition) and, to a lesser extent, tide intensity (or amplitude), suggesting that this is the most important forcing mechanism causing their generation (as previous authors had pointed out, [32,36]. On the other hand, and contrary to expectations, none of the other variables studied (wind intensity and direction, seasonality, spring-neap cycle) seem to show a significant effect. However, it should not be forgotten that submesoscale structures are 3D structures and, in this work, we are only observing their 2D projection on the surface, so it cannot be concluded that these variables do not affect other aspects of the formation or size of the structures in any way, such as the mixed layer depth or vertical flows associated with this dynamic. Nevertheless, data obtained from this analysis could even be useful to enhance zonal models, adjusting in situ parameters such as the current velocity, salinity, temperature, etc., which are determinant in the study of dispersion in water [91], as in the case of oil spill mitigation models, aggregation of surface floating material [33], or detection of coastal upwelling areas [32], or just as a tool to understand the presence and distribution of marine biodiversity related transport in the PIMCPA.

Optical satellite images have provided information at a spatial scale fine enough, and over a broad coastal area, that allowed relating submesoscale structures with their oceanographic forcing factors. Considering the time series extent of the Landsat images (although with some variations in their spatial resolution), retrospective studies of several decades could be carried out in the future to observe the long-term variation of the dynamics. In addition, future analysis could include not only images from other optical and available sensors, as Sentinel-2, to improve temporal resolution, but also in situ observation to detect the orbital velocities of these structures and learn about the vertical structure of the water column at various sectors of the PIMCPA.

Author Contributions: Conceptualization, O.M.O.-M., D.R.-P. and N.S.-C.; Data curation, O.M.O.-M. and J.P.P.; Formal analysis, N.S.-C.; Methodology, O.M.O.-M., J.P.P., D.R.-P. and N.S.-C.; Supervision, D.R.-P. and N.S.-C.; Validation, O.M.O.-M. and J.P.P.; Writing—original draft, O.M.O.-M. and N.S.-C.; Writing—review & editing, O.M.O.-M., J.P.P., D.R.-P. and N.S.-C. All authors have read and agreed to the published version of the manuscript.

Funding: This research was funded by the Argentine Ministerio de Ciencia Tecnología e Innovación under project PICT-2021-GRF-TI-00459 ("Estudio de procesos oceanográficos en el Mar Argentino mediante teledetección satelital, modelado numérico y datos in-situ") and the grant PIP 11220200102851CO ("Estudio de procesos oceanográficos de meso y submesoescala en el mar Argentino por medio de sensoramiento remoto, derivadores superficiales y simulaciones numéricas"), and by the Spanish Ministerio de Universidades and the UE Next Generation PRTR through a María Zambrano contract (budget application 33.50.460A.752).

Data Availability Statement: Publicly available datasets were analyzed in this study. This data can be found here: https://earthexplorer.usgs.gov (for Landsat-8 imagery; accessed on 26 February 2023), https://tpxows.azurewebsites.net (for TPXO tide model data; accessed 26 February 2023), https://cds.climate.copernicus.eu/cdsapp (for ERA5 data; accessed 26 February 2023).

Conflicts of Interest: The authors declare no conflict of interest.

References

1. Giraud, X.; Le Quéré, C.; Da Cunha, L.C. Importance of coastal nutrient supply for global ocean biogeochemistry. *Global Biogeochem. Cycles* **2008**, *22*, GB2025. [CrossRef]
2. Wolanski, E.; Hamner, W.M. Topographically controlled fronts in the ocean and their biological influence. *Science* **1988**, *241*, 177–181. [CrossRef] [PubMed]
3. Ivanov, A.Y.; Ginzburg, A.I. Oceanic eddies in synthetic aperture radar images. *J. Earth Syst. Sci.* **2002**, *111*, 281. [CrossRef]
4. Wolanski, E.; Imberger, J.; Heron, M.L. Island wakes in shallow coastal waters. *J. Geophys. Res. Ocean.* **1984**, *89*, 10553–10569. [CrossRef]
5. Gustafsson, Ö.; Gschwend, P.M. Hydrophobic organic compound partitioning from bulk water to the water/air interface. *Atmos. Environ.* **1998**, *33*, 163–167. [CrossRef]

6. Fossum, T.O.; Eidsvik, J.; Ellingsen, I.; Alver, M.O.; Fragoso, G.M.; Johnsen, G.; Mendes, R.; Ludvigsen, M.; Rajan, K. Information-driven robotic sampling in the coastal ocean. *J. Field Robot.* **2018**, *35*, 1101–1121. [CrossRef]
7. Zhu, L.; Suomalainen, J.; Liu, J.; Hyyppä, J.; Kaartinen, H.; Haggren, H. A review: Remote sensing sensors. In *Multi-Purposeful Application of Geospatial Data*; Rustamov, R.B., Hasanova, S., Zeynalova, M.H., Eds.; IntechOpen: London, UK, 2018; pp. 19–42. [CrossRef]
8. Cameron, H.L. Coastal studies by sequential air photography. *Can. Surv.* **1965**, *19*, 372–381. [CrossRef]
9. Stafford, D.B.; Langfelder, J. Air photo survey of coastal erosion. *Photogramm. Eng.* **1971**, *37*, 565–575.
10. Whitehead, H.; Payne, R. New techniques for assessing populations. *Mamm. Seas Rep.* **1978**, *3*, 189.
11. Baily, B.; Nowell, D. Techniques for monitoring coastal change: A review and case study. *Ocean Coast. Manag.* **1996**, *32*, 85–95. [CrossRef]
12. Stumpf, R.P. Applications of satellite ocean color sensors for monitoring and predicting harmful algal blooms. *Hum. Ecol. Risk Assess. An Int. J.* **2001**, *7*, 1363–1368. [CrossRef]
13. Riddick, C.A.L.; Hunter, P.D.; Dominguez Gómez, J.A.; Martinez-Vicente, V.; Présing, M.; Horváth, H.; Kovács, A.W.; Vörös, L.; Zsigmond, E.; Tyler, A.N. Optimal cyanobacterial pigment retrieval from ocean colour sensors in a highly turbid, optically complex lake. *Remote Sens.* **2019**, *11*, 1613. [CrossRef]
14. Chen, S.; Meng, Y.; Lin, S.; Xi, J. Remote Sensing of the Seasonal and Interannual Variability of Surface Chlorophyll-a Concentration in the Northwest Pacific over the Past 23 Years (1997–2020). *Remote Sens.* **2022**, *14*, 5611. [CrossRef]
15. Robinson, I.S. *Measuring the Oceans from Space: The Principles and Methods of Satellite Oceanography*; Springer Science & Business Media: Berlin/Heidelberg, Germany, 2004.
16. Horstmann, J.; Koch, W. Measurement of ocean surface winds using synthetic aperture radars. *IEEE J. Ocean. Eng.* **2005**, *30*, 508–515. [CrossRef]
17. Fore, A.G.; Yueh, S.H.; Tang, W.; Stiles, B.W.; Hayashi, A.K. Combined active/passive retrievals of ocean vector wind and sea surface salinity with SMAP. *IEEE Trans. Geosci. Remote Sens.* **2016**, *54*, 7396–7404. [CrossRef]
18. Zhou, L.; Zheng, G.; Li, X.; Yang, J.; Ren, L.; Chen, P.; Zhang, H.; Lou, X. An improved local gradient method for sea surface wind direction retrieval from SAR imagery. *Remote Sens.* **2017**, *9*, 671. [CrossRef]
19. Cantón Garbin, M.; Guerra, A.H. La Teledetección de Los Océanos Desde El Espacio. *Rev. Española Fis.* **2008**, *5*, 8–14. (In Spanish)
20. Groom, S.; Sathyendranath, S.; Ban, Y.; Bernard, S.; Brewin, R.; Brotas, V.; Brockmann, C.; Chauhan, P.; Choi, J.; Chuprin, A.; et al. Satellite ocean colour: Current status and future perspective. *Front. Mar. Sci.* **2019**, *6*, 485. [CrossRef]
21. Chander, G.; Markham, B.L.; Helder, D.L. Summary of current radiometric calibration coefficients for Landsat MSS, TM, ETM+, and EO-1 ALI sensors. *Remote Sens. Environ.* **2009**, *113*, 893–903. [CrossRef]
22. Hemati, M.; Hasanlou, M.; Mahdianpari, M.; Mohammadimanesh, F. A systematic review of landsat data for change detection applications: 50 years of monitoring the earth. *Remote Sens.* **2021**, *13*, 2869. [CrossRef]
23. Aleskerova, A.; Kubryakov, A.; Stanichny, S.; Medvedeva, A.; Plotnikov, E.; Mizyuk, A.; Verzhevskaia, L. Characteristics of topographic submesoscale eddies off the Crimea coast from high-resolution satellite optical measurements. *Ocean Dyn.* **2021**, *71*, 655–677. [CrossRef]
24. Hong, T.T.M.; Park, Y.; Choi, J.M.; Thi, T.; Hong, M.; Park, Y. Divergence Observation in a Mesoscale Eddy during Chla Bloom Revealed in Submesoscale Satellite Currents. *Remote Sens.* **2023**, *15*, 995. [CrossRef]
25. Pattiaratchi, C.; James, A.; Collins, M. Island wakes and headland eddies: A comparison between remotely sensed data and laboratory experiments. *J. Geophys. Res.* **1987**, *92*, 783. [CrossRef]
26. Thomas, L.N.; Tandon, A.; Mahadevan, A. Submesoscale processes and dynamics. In *Ocean Modeling in an Eddying Regime*; Hecht, M.W., Hasumi, H., Eds.; AGU Books: Washington, DC, USA, 2008. [CrossRef]
27. Sathyendranath, S. (Ed.) *Remote Sensing of Ocean Colour in Coastal, and Other Optically-Complex, Waters*; International Ocean Colour Coordinating Group (IOCCG): Dartmouth, NS, Canada, 2000. [CrossRef]
28. Alldredge, A.L.; Hamner, W.M. Recurring aggregation of zooplankton by a tidal current. *Estuar. Coast. Mar. Sci.* **1980**, *10*, 31–37. [CrossRef]
29. Lévy, M.; Franks, P.J.S.; Smith, K.S. The role of submesoscale currents in structuring marine ecosystems. *Nat. Commun.* **2018**, *9*, 4758. [CrossRef]
30. Fadeev, E.; Wietz, M.; von Appen, W.-J.; Iversen, M.H.; Nöthig, E.-M.; Engel, A.; Grosse, J.; Graeve, M.; Boetius, A. Submesoscale physicochemical dynamics directly shape bacterioplankton community structure in space and time. *Limnol. Oceanogr.* **2021**, *66*, 2901–2913. [CrossRef]
31. Schnack, E.; Pousa, J.; Bértola, G.; Isla, F. Argentina. In *Encyclopedia of the World's Coastal Landforms*; Bird, E.C.F., Ed.; Springer: Dordrecht, The Netherlands, 2010. [CrossRef]
32. Gagliardini, D.A.; Amoroso, R.O.; Dell'Arciprete, O.P.; Yorio, P.; Orensanz, J.M. Detection of small-scale coastal oceanographic processes through LANDSAT-TM/ETM+ images: Implications for the study of biological processes along the Patagonian coasts of Argentina. *Gayana (Concepción)* **2004**, *68*, 194–200. [CrossRef]
33. Capet, X.; Campos, E.J.; Paiva, A.M. Submesoscale activity over the Argentinian shelf. *Geophys. Res. Lett.* **2008**, *35*, L15605. [CrossRef]
34. Tonini, M.H.; Palma, E.D. Circulación residual y vorticidad mareal en los golfos norpatagónicos. *Mecánica Comput.* **2009**, *28*, 2851–2867.

35. Tonini, M.H.; Palma, E.D. Tidal dynamics on the North Patagonian Argentinean gulfs. *Estuar. Coast. Shelf Sci.* **2017**, *189*, 115–130. [CrossRef]
36. Pisoni, J.P.; Tonini, M.H.; Glembocki, N.; Romero, S. Headland eddies and island wakes over the Argentine Patagonian coast. *Remote Sens. Lett.* 2023; submitted.
37. Retana, M.V.; Lewis, M.N. Suitable habitat for marine mammals during austral summer in San Jorge Gulf, Argentina. *Rev. Biol. Mar. Oceanogr.* **2017**, *52*, 275–288. [CrossRef]
38. Yorio, P. Marine protected areas, spatial scales, and governance: Implications for the conservation of breeding seabirds. *Conserv. Lett.* **2009**, *2*, 171–178. [CrossRef]
39. Crespo, E.A.; Pedraza, S.N.; Dans, S.L.; Koen Alonso, M.; Reyes, L.M.; García, N.A.; Coscarella, M.; Schiavini, A.C.M. Direct and indirect effects of the highseas fisheries on the marine mammal populations in the northern and central Patagonian coast. *J. Northwest Atl. Fish. Sci.* **1997**, *22*, 189–207. [CrossRef]
40. Borboroglu, P.G.; Yorio, P.; Boersma, P.D.; Del Valle, H.; Bertellotti, M. Habitat use and breeding distribution of Magellanic penguins in northern San Jorge Gulf, Patagonia, Argentina. *Auk* **2002**, *119*, 233–239. [CrossRef]
41. Yorio, P.; Quintana, F.; Dell'arciprete, P.; González-Zevallos, D.; DELL'ARCIPRETE, P.; Gonzalez-Zevallos, D. Spatial overlap between foraging seabirds and trawl fisheries: Implications for the effectiveness of a marine protected area at Golfo San Jorge, Argentina. *Bird Conserv. Int.* **2010**, *20*, 320–334. [CrossRef]
42. Sánchez-Carnero, N.; Rodríguez-Pérez, D. A sea bottom classification of the Robredo area in the Northern San Jorge Gulf (Argentina). *Geo-Mar. Lett.* **2021**, *41*, 12. [CrossRef]
43. Fernández, M.; Carreto, J.I.; Mora, J.; Roux, A. Physico-chemical characterization of the benthic environment of the Golfo San Jorge, Argentina. *J. Mar. Biol. Assoc. UK* **2005**, *85*, 1317–1328. [CrossRef]
44. Marinho, C.H.; Gil, M.N.; Esteves, J.L. Distribution and origin of trace metals in sediments of a marine park (Northern San Jorge Gulf) from Argentina. *Mar. Pollut. Bull.* **2013**, *72*, 260–263. [CrossRef] [PubMed]
45. Latorre, M.P.M.P.; Schloss, I.R.; Almandoz, G.O.; Lemarchand, K.; Flores-Melo, X.; Massé-Beaulne, V.; Ferreyra, G.A. Mixing processes at the pycnocline and vertical nitrate supply: Consequences for the microbial food web in San Jorge Gulf, Argentina. *Oceanography* **2018**, *31*, 50–59. [CrossRef]
46. Díaz, P.; López Gappa, J.J.; Piriz, M.L. Symptoms of eutrophication in intertidal macroalgal assemblages of Nuevo Gulf (Patagonia, Argentina). *Bot. Mar.* **2002**, *45*, 267–273. [CrossRef]
47. Torres, A.I.; Paparazzo, F.E.; Williams, G.N.; Rivas, A.L.; Solís, M.E.; Esteves, J.L. Dynamics of macronutrients in the San Jorge Gulf during spring and summer. *Oceanography* **2018**, *31*, 25–32. [CrossRef]
48. Desiage, P.-A.; Montero-Serrano, J.-C.; St-Onge, G.; Crespi-Abril, A.C.; Giarratano, E.; Gil, M.N.; Haller, M.J. Quantifying sources and transport pathways of surface sediments in the Gulf of San Jorge, central Patagonia (Argentina). *Oceanography* **2018**, *31*, 92–103. [CrossRef]
49. Tonini, M.; Palma, E.; Rivas, A. Modelo de alta resolución de los Golfos Patagónicos. *Mecánica Comput.* **2006**, *XXV*, 1441–1460.
50. Matano, R.; Palma, E. Seasonal Variability of the Oceanic Circulation in the Gulf of San Jorge, Argentina. *Oceanography* **2018**, *31*, 16–24. [CrossRef]
51. Palma, E.D.; Matano, R.P.; Tonini, M.H.; Martos, P.; Combes, V. Dynamical analysis of the oceanic circulation in the Gulf of San Jorge, Argentina. *J. Mar. Syst.* **2020**, *203*, 103261. [CrossRef]
52. Fernández, M.; Roux, A.; Fernández, E.; Caló, J.; Marcos, A.; Aldacur, H. Grain-size analysis of surficial sediments from Golfo San Jorge, Argentina. *J. Mar. Biol. Assoc. UK* **2003**, *83*, 1193–1197. [CrossRef]
53. Rodriguez-Perez, D.; Sanchez-Carnero, N. Multigrid/Multiresolution Interpolation: Reducing Oversmoothing and Other Sampling Effects. *Geomatics* **2022**, *2*, 236–253. [CrossRef]
54. Bertuche, D.; Fischbach, C.; Roux, A.; Fernandez, M.; Pinero, R. Langostino (Pleoticus muelleri). In *Síntesis del Estado de las Pesquerías Marítimas Argentinas y de la Cuenca del Plata. Años 1997–1998, con la Actualización de 1999*; Bezzi, S., Akselman, R., Boschi, E., Eds.; INIDEP: Mar del Plata, Argentina, 2000; pp. 179–190. ISBN 987-96244-7-5. (In Spanish)
55. Nievas, M.L.; Esteves, J.L. *Relevamiento de Actividades Relacionadas con la Explotación de Petróleo en zona Costera Patagónica y datos Preliminares Sobre Residuos de Hidrocarburos en Puertos*; Fundación Patagonia Natural: Puerto Madryn, Argentina, 2007; ISBN 978-987-97411-5-3. Available online: http://hdl.handle.net/11336/136664 (accessed on 26 February 2023). (In Spanish)
56. Gongora, M.E.; Gonzalez Zevallos, D.; Pettovello, A.; Mendia, L. Characterization of the main fisheries in San Jorge Gulf, Patagonia, Argentina/Caracterizacion de las principales pesquerias del golfo San Jorge Patagonia, Argentina. *Lat. Am. J. Aquat. Res.* **2012**, *40*, 1–11. [CrossRef]
57. Akselman, R. Estudios Ecologicos en el Golfo San Jorge y Adyacencias (Atlantico Sudoccidental). Distribucion, Abundancia Y Variacion Estacional del Fitoplancton en Relacion a Factores Fisico-Quimicos Y la Dinamica Hidrologica. Ph.D. Thesis, Universidad De Buenos Aires, Buenos Aires, Argentina, 1996.
58. Flores-Melo, X.; Schloss, I.R.; Chavanne, C.; Almandoz, G.O.; Latorre, M.; Ferreyra, G.A. Phytoplankton ecology during a spring-neap tidal cycle in the southern tidal front of san jorge gulf, patagonia. *Oceanography* **2018**, *31*, 104–112. [CrossRef]
59. Dans, S.L.; Cefarelli, A.O.; Galván, D.; Gongora, M.E.; Martos, P.; Varisco, M.M.A.; Alvarez Colombo, G.L.; Blanc, S.; Bos, P.; Bovcon, N.D.; et al. El golfo San Jorge como área prioritaria de investigación, manejo y conservación en el marco de la iniciativa Pampa Azul. *Rev. Cienc. Investig.* **2021**, *71*, 21–43. (In Spanish)

60. Pisoni, J.P.; Rivas, A.L.; Tonini, M.H. Coastal upwelling in the San Jorge Gulf (Southwestern Atlantic) from remote sensing, modelling and hydrographic data. *Estuar. Coast. Shelf Sci.* **2020**, *245*, 106919. [CrossRef]
61. Rivas, A.L.; Pisoni, J.P. Identification, characteristics and seasonal evolution of surface thermal fronts in the Argentinean Continental Shelf. *J. Mar. Syst.* **2010**, *79*, 134–143. [CrossRef]
62. Glembocki, N.G.; Williams, G.N.; Góngora, M.E.; Gagliardini, D.A.; Orensanz, J.M. (Lobo). Synoptic oceanography of San Jorge Gulf (Argentina): A template for Patagonian red shrimp (Pleoticus muelleri) spatial dynamics. *J. Sea Res.* **2015**, *95*, 22–35. [CrossRef]
63. Pessacg, N.; Blázquez, J.; Lancelotti, J.; Solman, S. Climate changes in coastal areas of Patagonia: Observed trends and future projections. In *Global Change in Atlantic Coastal Patagonian Ecosystems: A Journey Through Time*; Springer: Berlin/Heidelberg, Germany, 2022; pp. 13–42.
64. Labraga, J.C. Extreme winds in the Pampa del Castillo Plateau, Patagonia, Argentina, with reference to wind farm settlement. *J. Appl. Meteorol. Climatol.* **1994**, *33*, 85–95. [CrossRef]
65. Irons, J.R.; Dwyer, J.L.; Barsi, J.A. The next Landsat satellite: The Landsat data continuity mission. *Remote Sens. Environ.* **2012**, *122*, 11–21. [CrossRef]
66. Egbert, G.D.; Erofeeva, S.Y. Efficient inverse modeling of barotropic ocean tides. *J. Atmos. Ocean. Technol.* **2002**, *19*, 183–204. [CrossRef]
67. Hersbach, H.; Bell, B.; Berrisford, P.; Hirahara, S.; Horányi, A.; Muñoz-Sabater, J.; Nicolas, J.; Peubey, C.; Radu, R.; Schepers, D.; et al. The ERA5 global reanalysis. *Q. J. R. Meteorol. Soc.* **2020**, *146*, 1999–2049. [CrossRef]
68. Chavez Jr, P.S. An improved dark-object subtraction technique for atmospheric scattering correction of multispectral data. *Remote Sens. Environ.* **1988**, *24*, 459–479. [CrossRef]
69. Hedley, J.D.; Harborne, A.R.; Mumby, P.J. Simple and robust removal of sun glint for mapping shallow-water benthos. *Int. J. Remote Sens.* **2005**, *26*, 2107–2112. [CrossRef]
70. Hochberg, E.J.; Andréfouët, S.; Tyler, M.R. Sea surface correction of high spatial resolution ikonos images to improve bottom mapping in near-shore environments. *IEEE Trans. Geosci. Remote Sens.* **2003**, *41*, 1724–1729. [CrossRef]
71. Vidhya, G.R.; Ramesh, H. Effectiveness of contrast limited adaptive histogram equalization technique on multispectral satellite imagery. In Proceedings of the International Conference on Video and Image Processing, Beijing, China, 17–20 September 2017; pp. 234–239. [CrossRef]
72. Dong, C.; McWilliams, J.C.; Liu, Y.; Chen, D. Global heat and salt transports by eddy movement. *Nat. Commun.* **2014**, *5*, 3294. [CrossRef] [PubMed]
73. Fedorov, K.N.; Ginsburg, A.I. Mushroom-like currents (vortex dipoles): One of the most widespread forms of non-stationary coherent motions in the ocean. In *Elsevier Oceanography Series*; Elsevier: Amsterdam, The Netherlands, 1989; Volume 50, pp. 1–14.
74. Gagliardini, D.A. Medium Resolution Microwave, Thermal and Optical Satellite Sensors: Characterizing Coastal Environments Through the Observation of Dynamical Processes. In *Remote Sensing of the Changing Oceans*; Tang, D., Ed.; Springer: Berlin/Heidelberg, Germany, 2011; pp. 251–277. [CrossRef]
75. Munk, W.; Armi, L.; Fischer, K.; Zachariasen, F. Spirals on the sea. *Proc. R. Soc. London. Ser. A Math. Phys. Eng. Sci.* **2000**, *456*, 1217–1280. [CrossRef]
76. Rossby, C.-G. Solenoidal circulations resulting from lateral mixing. *Eos Trans. Am. Geophys. Union* **1938**, *19*, 159–162. [CrossRef]
77. Dong, C.; Cao, Y.; McWilliams, J.C. Island wakes in shallow water. *Atmos.-Ocean.* **2018**, *56*, 96–103. [CrossRef]
78. Palacios, D.M. Seasonal patterns of sea-surface temperature and ocean color around the Galápagos: Regional and local influences. *Deep Sea Res. Part II Top. Stud. Oceanogr.* **2004**, *51*, 43–57. [CrossRef]
79. Chen, S.; Hu, C. Estimating sea surface salinity in the northern Gulf of Mexico from satellite ocean color measurements. *Remote Sens. Environ.* **2017**, *201*, 115–132. [CrossRef]
80. Westberry, T.K.; Silsbe, G.M.; Behrenfeld, M.J. Gross and net primary production in the global ocean: An ocean color remote sensing perspective. *Earth-Sci. Rev.* **2023**, *237*, 104322. [CrossRef]
81. Choi, J.; Park, Y.-G.; Kim, W.; Kim, Y.H. Characterization of submesoscale turbulence in the east/japan sea using geostationary ocean color satellite images. *Geophys. Res. Lett.* **2019**, *46*, 8214–8223. [CrossRef]
82. Li, G.; He, Y.; Liu, G.; Zhang, Y.; Hu, C.; Perrie, W. Multi-sensor observations of submesoscale eddies in coastal regions. *Remote Sens.* **2020**, *12*, 711. [CrossRef]
83. Fu, L.-L.; Ferrari, R. Observing oceanic submesoscale processes from space. *Eos Trans. Am. Geophys. Union* **2008**, *89*, 488. [CrossRef]
84. Cai, L.; Zhou, M.; Liu, J.; Tang, D.; Zuo, J.; Hamze-ziabari, S.M.; Foroughan, M.; Lemmin, U.; Barry, D.A.; Jolliff, J.K.; et al. HY-1C observations of the impacts of Islands on suspended sediment distribution in Zhoushan coastal waters, China. *Remote Sens.* **2020**, *12*, 1766. [CrossRef]
85. Kubryakov, A.A.; Lishaev, P.N.; Chepyzhenko, A.I.; Aleskerova, A.A.; Kubryakova, E.A.; Medvedeva, A.V.; Stanichny, S.V. Impact of Submesoscale Eddies on the Transport of Suspended Matter in the Coastal Zone of Crimea Based on Drone, Satellite, and In Situ Measurement Data. *Oceanology* **2021**, *61*, 159–172. [CrossRef]
86. DiGiacomo, P.M.; Holt, B. Satellite observations of small coastal ocean eddies in the Southern California Bight. *J. Geophys. Res. Ocean.* **2001**, *106*, 22521–22543. [CrossRef]

87. Karimova, S. Spiral eddies in the Baltic, Black and Caspian seas as seen by satellite radar data. *Adv. Sp. Res.* **2012**, *50*, 1107–1124. [CrossRef]
88. Lavrova, O.; Serebryany, A.; Bocharova, T.; Mityagina, M. Investigation of fine spatial structure of currents and submesoscale eddies based on satellite radar data and concurrent acoustic measurements. In Proceedings of the Remote Sensing of the Ocean, Sea Ice, Coastal Waters, and Large Water Regions, Edinburgh, UK, 26–27 September 2012; Volume 85320. [CrossRef]
89. Kozlov, I.E.; Artamonova, A.V.; Manucharyan, G.E.; Kubryakov, A.A. Eddies in the Western Arctic Ocean from spaceborne SAR observations over open ocean and marginal ice zones. *J. Geophys. Res. Ocean.* **2019**, *124*, 6601–6616. [CrossRef]
90. Gurova, E.; Chubarenko, B. Remote-sensing observations of coastal sub-mesoscale eddies in the south-eastern Baltic. *Oceanologia* **2012**, *54*, 631–654. [CrossRef]
91. Ginzburg, A.I.; Bulycheva, E.V.; Kostianoy, A.G.; Solovyev, D.M. On the role of vortices in the transport of oil pollution in the Southeastern Baltic Sea (according to satellite monitoring). *Sovrem. Probl. Distantsionnogo Zo. Zemli Iz Kosm.* **2015**, *12*, 149–157.